Multi-scale constitutive model and computational framework for the design of ultra-high strength, high toughness steels

Su Hao [a,b,*], Wing Kam Liu [b,*], Brian Moran [b], Franck Vernerey [b], Gregory B. Olson [a]

[a] D a , Ma ,a a Sç c E , , , N U , , , 2145 S , a R a , E a , , IL 60208-3111, USA

[b] D a , M c a ,ca E , , , T T c , , ,ca I , , N U , , , 2145 S , a R a , E a , , IL 60208-3111, USA

Received 5 June 2003; received in revised form 16 October 2003; accepted 2 December 2003

A s t t

A multi-scale hierarchical constitutive model is developed for establishing the relationship between quantum mechanical, micromechanical, and overall strength/toughness properties in steel design. Focused on the design of ultra-high strength, high toughness steels, a two-level cell model is used to represent two groups of hard particles (inclusions) in an alloy matrix which is characteristic of such Fe-based alloys. Primary inclusion particles, which are greater than a micron in size, are handled by a microcell. Secondary inclusion particles which are tens of nanometers in size are modeled by a sub-microcell. In the sub-microcell, the matrix constitutive behavior is given by quantum mechanics computation of bcc-iron calibrated according to experiments. In the microcell, the matrix constitutive behavior is given by the stress–strain response of the sub-microcell, characterized by a plastic flow potential based on the numerical simulation of the representative cell. In turn, the plastic flow potential generated by the stress–strain response of the microcell is used as the constitutive response at the continuum macro level for simulation of ductile fracture and for the assessments of toughness. The interfacial debonding between the matrix and the primary and the secondary inclusion particles are modeled using decohesion potentials computed through quantum mechanics calculation together with a mechanical model of normal separation and gliding induced dislocation, which also provides quantitative explanations why practice strength of a steel is much lower than the atomic separation force and how plasticity occurs in steels.

The ductile fracture simulations on an ASTM standard center cracked specimen lead to the generation, for the first time, of a toughness, strength, adhesion diagram based on computer simulation and which establishes the relationship between alloy matrix strength, interfacial decohesion energy, and fracture toughness.

K , :

1. Introduction

One of the principal objectives of micro/nanomechanics of materials is to account for the observed phenomena and properties of macroscopic solid bodies, such as strength and fracture toughness of steels, on the basis of the quantum mechanical theory of the behavior of atomic particles. Success will have been achieved when it becomes possible to calculate the quantities that describe the constitution of materials and their response to alterations of macroscopic mechanical boundary conditions from the knowledge of the component elements and their hierarchical structures from atomistic–electronic scales to micro- and macroscales. This is particularly important for steel design.

For this purpose, the difficulties and complexity originate in the substantial differences in philosophy and viewpoints between conventional continuum mechanics and quantum theory. In the former, the solution of a boundary value problem is uniquely determined based on Newton's laws when initial and boundary conditions are given; whereas the Heisenberg uncertainty principle, the cornerstone of quantum mechanics, indicates that motion of a particle is characterized by wave solutions of Schödinger's equation and the intensity of wave solutions defines the ''probability density'' for the position of this particle. For mechanical engineers, the challenges lie in how to establish the relationship between a continuum mechanical system and its atomistic–electronic structure and how to constitute a unified framework that bridges the mechanisms from different scales. These are the key-issues in the ONR project ''cybersteel2020'' [1] towards the predictive design of novel steels to combine high strength and fracture toughness.

Both strength and fracture toughness are the key property-indices for steels. Although advanced technology currently provides many ways to achieve either high strength or high toughness, respectively, in steel through manufacturing processes, it remains a challenge to achieve both of them simultaneously. This is because the toughness characterizes the capability of a material against fracture at a crack tip local. The difference between the local and the global properties reflects the natural heterogeneity of the microstructure of steels. The design of steels seeks to achieve desirable micro/nanostructures with optimized properties through alloy component/phase selection and metallurgical processes based on quantitative understanding of controlling mechanisms and the relationships among these at different scales.

In this paper, a bottom-up computational methodology has been proposed to establish a hierarchical multi-physics constitutive model that builds up the relationships among the macroscale properties, micro-

''ductile fracture simulator'' by the authors, to support quantitative tradeo analysis in microstructural optimization for fracture toughness.

5. A toughness–strength–adhesion diagram has been obtained for steel design, which establishes the relationship among alloy matrix strength, inclusion adhesion interfacial energy and fracture toughness. To the authors' knowledge this is the first computer generated design diagram for engineering application.

This paper is organized as follows: In Section 2 we introduce the hierarchical model. Section 3 describes the quantum physics analysis and the bridge to continuum mechanics. The Quasi-particle dynamics approach is introduced in Section 4. A unified multi-physics thermodynamic framework in continuum mechanics and a two-level cell representation at sub-micro- and microscales are derived in Section 5, which lead to a hierarchical
presented in Section 6. As a con/% e1clusion, a toughness–strength–adhesion diagram is developed. This diagram, together with the hierarchical con/% e1stitutive model and
''ductile fracture simulator'' presented in Section 7.

2. IC' t ' pp '

Like all
generally Aq/% e1nsists of an alloy matrix with se

the iron matrix and the interfacial behavior between the matrix and the inclusions, leading in turn to the continuum mechanics decohesion potentials for di erent interfaces and alloy matrices. A continuum mechanics analysis is applied in the unit cell representation with primary particles, which we call ‘‘microscale cell model’’. A ‘‘Quasi-particle dynamics approach’’ is developed for the cell representation with secondary particles, which is termed ‘‘sub-microcell model’’. At the quantum scale, the sub-atomic

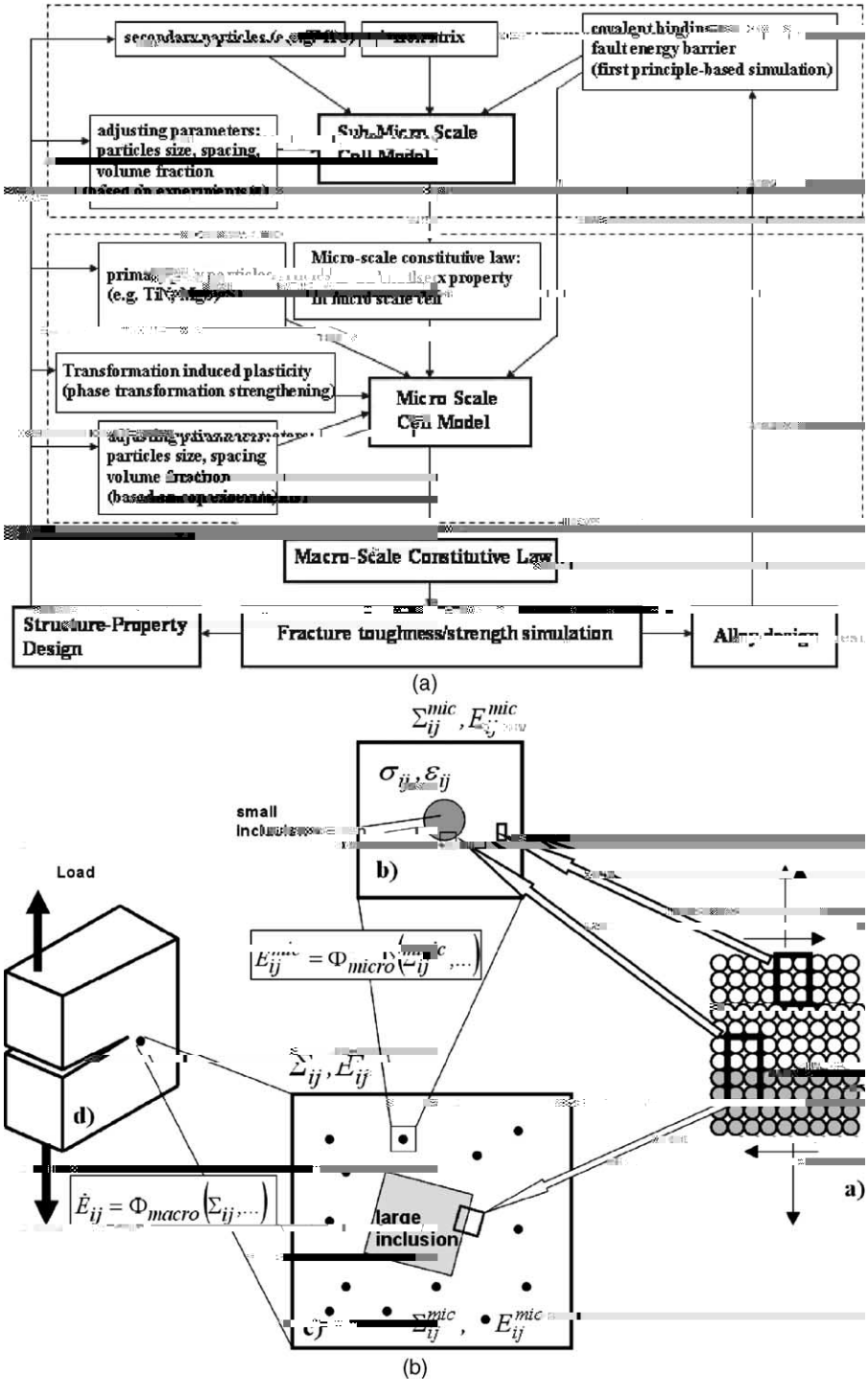

Fig. 2. (a) The flow chart of the proposed approach. (b) An illustration of the proposed hierarchical model that links : the quantum scale, : sub-microscale, : microscale, : macroscale.

which may trigger other defects, such as the motion of dislocations along interacting slip planes. Rice's criterion [2] states that dislocation motion will be activated when the energy barrier, γ_{US}, against unstable sliding is smaller than the cleavage surface energy, γ_F, which provides a basis for describing the competition between these two mechanisms. The mathematical expression of Rice's criterion is:

$$\frac{\gamma_F}{\gamma_{US}}\ _R > 1, \qquad (3.3)$$

where $_R$ is a function of the average lattice elastic stress and the angle ϕ between the slip-plane and the newly-created surface, and $_R < 1$. When dislocation induced sliding occurs, the relation between the total system energy E_S and sliding separation $_S$ per dislocation can be writtenlqPc eD9qPFqF%ePP6(1–AA)xlPAxdFnr]+

For a system such as the Fe/TiC interface shown in Fig. 3a, the following failure modes may occur:

1. normal and sliding separations in Fe;
2. normal and sliding separations in the TiC;
3. Fe/TiC interfacial debonding.

The TiC, as a ceramic, has a much higher coherent strength than Fe [15], so the failure mode 2 is excluded in this analysis.

Both the normal separation and shear sliding in iron matrix have been studied in this paper. We have computed the $\langle \bar{1}\bar{1}1 \rangle$ shear fault energy on the $\{1\bar{1}1\}$ plane, the normal separation of Fe–Ti site of the

most preferred binding surfaces of both sides with three possible arrangements: Fe–C site, Fe–Ti site, and Fe–TiC saddle point site (see Fig. 3b).

The study of the coherent Fe–TiC interface was first performed by Freeman's group [17] using FLAPW [21]. In this paper the simulation and calibration of (3.1) and (3.2) of the sub-atomic cell of $f001g_{bcc}^{Fe}kf001g_{fcc}^{TiC}$ decohesion is computed. The interfacial debonding energies are listed in Table 1.

It should be pointed out that the primitive model of Fig. 3a actually represents the interface of a periodically repeated Fe/TiC layered structure. The height of each layer is twice times of the atoms layers plotted in the figure. In this primitive cell analysis the e ects of layer overlay are omitted.

3.2.1.2. D ç .. . a . (1 1 1). bcc-. . A sub-atomic cell is developed as illustrated in Fig. 4a, where the primitive vectors take the form

$$^{-}¼ \square\hat{}\ þ\ \hat{}, \quad ^{-}¼ \square\hat{}\ þ\ \hat{}, \quad ^{-}¼\ \hat{}\ þ\ \hat{}\ þ\ \hat{}, \qquad ð3.6Þ$$

which are originated at $ð\hat{}, 0, 0Þ$. Presuming the six outer surfaces of the cell to be rigid, periodic boundary

reproducible throughout space. The $12\times12\times1$ k-point mesh with Monkhorst and Pack scheme is applied in the simulations.

3.2.1.3. R . The results are summarized in Table 1. The corresponding computed energy-separation curves are plotted in Fig. 4b.

3.2.2. G

The stacking fault energy barrier γ_{US} is a crucial parameter for materials, as Eq. (3.3) indicates that the ratio of

where q varies from 0 to 1, representing the gliding induced sliding; and

$$g\eth q\text{Þ} \text{¼} \begin{cases} 1 & q < 0.25, \\ \dfrac{3 \square 4q}{2} & 0.25 \leqslant q < 0.75, \\ 0 & q \geqslant 0.75. \end{cases}$$

The computed energy-sliding relation is plotted in Fig. 6, which demonstrates the energy barrier γ_{US} for the motion of $\frac{a}{8}\langle 1\bar{1}0\rangle$ is about 0.31 J/M^2 and the γ_{US} for –

3.3. A a ac ba N a a a c a c a

Needleman [23] developed an interface cohesive model that defines the normal traction δ_N and tangential traction δ_T along the interface through a potential $\Psi_{\text{interface}}$

$$_N \frac{\partial \Psi_{\text{interface}}}{}$$

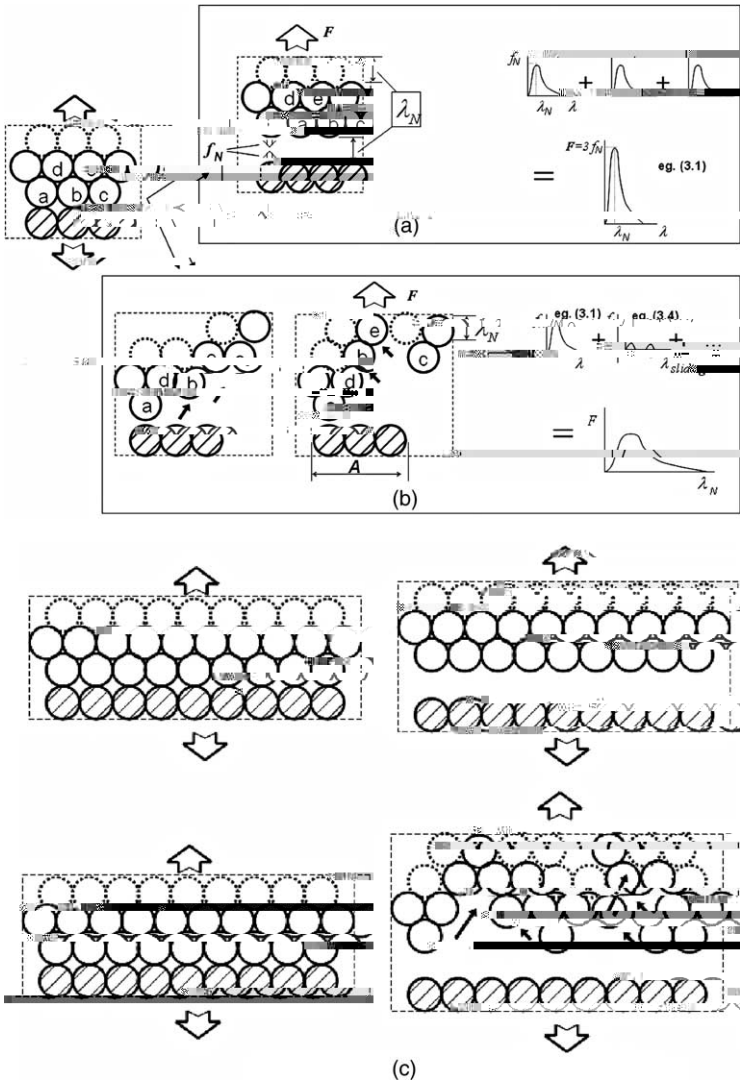

Fig. 7. Normal separation and sliding induced separation: (a) pure normal separation; (b) mixed separation–separation strength weakens and (c) a dislocation induced sliding may cause a zigzag morphology at fracture surface.

By substituting (3.12) into (3.11), the latter becomes

$$\Psi_N \frac{1}{4} 2\gamma_F E_N^{\square}\left(\left[\frac{N \square N0}{l_{TF}} \right] \right) \qquad \text{ð3.13Þ}$$

and

$$\Psi_T \frac{1}{4} E_{\gamma}. \qquad \text{ð3.14Þ}$$

In this paper the e ect of dislocation induced atomic vibration (dislocation–phonon interaction) is omitted.

3.5. G ą b ẹ a , a ,,

An Fe–TiC interface can be viewed as a grain boundary. This is because in practices it is non-trivial to control all surfaces of a TiC particle to be perfectly coherent to alloy matrix. The vicinity of a grain boundary interface can be represented by three regions: grain A, grain B, and an interfacial zone h; as illustrated in Fig. 8. Irregularities such as misfit in lattice constants, mismatch in atomistic properties and crystal orientations, molar fraction of the solute, and the free volume in h, may change the energy-separation potentials (3.13) and (3.14) significantly [25].

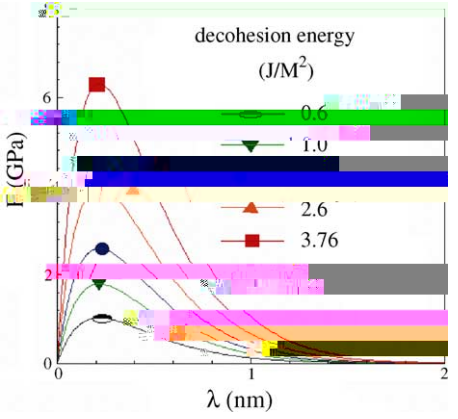

Fig. 9. Interfacial metallic debonding/decohesion law.

analysis [23,24] indicates that the maximum separation stress between a hard inclusion and an iron matrix is approximately ð1 þ 3Þ flow.

Finally, we obtained the normal traction-separations for the Fe–TiC interface which are plotted in Fig. 9 using ¼ 1/5 to calibrate (3.13) based on the results in Fig. 4b and Table 1. The curve with the maximum peak stress is corresponding to the Fe–C site separation while the one with the lowest peak stress is corresponding to the Fe–Ti site separation.

4. [illegible] [1]

As mentioned in Section 2, the secondary particles in ultra high strength steel are on the order of tens nanometers in size. Materials decohesion and fracture at this scale may depend strongly on atomistic properties, such as crystal periodicity and orthogonal anisotropy. Molecular dynamics (MD) is an appropriate method to bridge the quantum physics to continuum mechanical analysis at this scale.

The application of molecular dynamics is hampered by the computational demands of simulating a su ciently large number of atoms to represent the physical phenomenon of interest. The interatomic distances in a crystal are at the order of Angstroms. Hence, a simulation of a 3D cell model with the dimension of hundreds nanometers requires about 10^9 atoms. A laboratory specimen for fracture toughness is usually on the scale of centimeters. For such a specimen, an ''exact'' 3D simulation using molecular dynamics or other atomistic methods requires a model that contains about 10^{20} atoms, which is beyond current computational limits. This motivated the development of the ''Quasi-particle dynamics approach''; for short, ''Particle Dynamics''.

The basic idea of ''Quasi-particle dynamics approach'' is to represent an atomic system as a particle system through lumping fixed number of atoms into a super-atom, which we call a ''particle'', while preserving the essential properties of the atomic system via a proposed ''equivalent sti ness rule''. This rule requires that the particle system has the same crystal structure and sti ness coe cients as the original atomic system but with a larger inter-particle spacing that is determined from the scale of interest, see Fig. 10b and c. The original physics is preserved through transforming the inter-atomic potential (Fig. 10a) into

[1] This method is also termed ''Particle Dynamics'' in other publications of the authors.

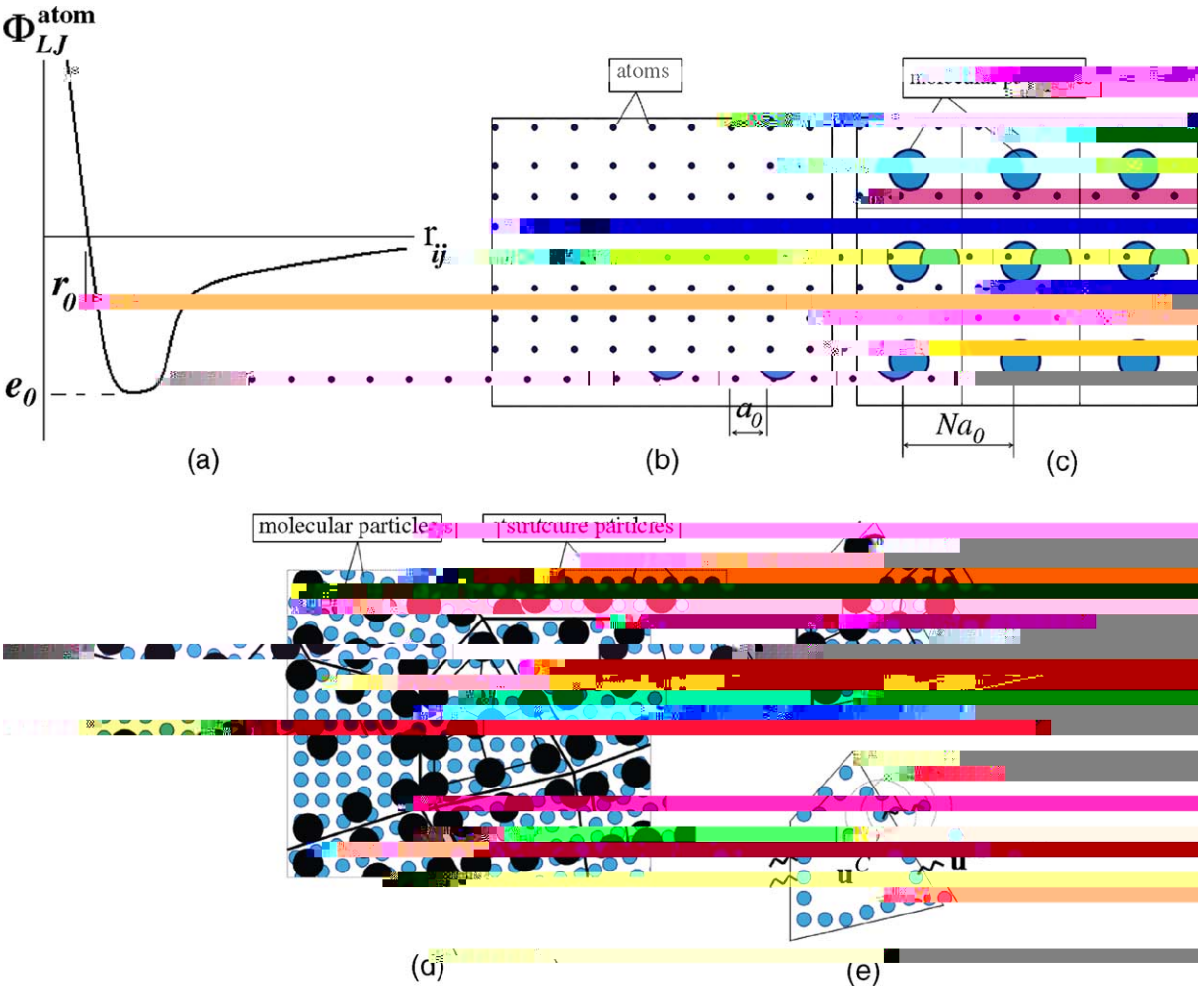

Fig. 10. Quasi-particle dynamics approach (particle dynamics): (a) conventional Lennard–Jones potential; (b) an atomic system with the equilibrium interatomic distance a_0; (c) a particle system with the equilibrium inter-particle distance Na_0; the particles at this scale are termed as ''quasi-particles''; (d) the structural particle system where each structural particle is lumped into several quasi particles; all structural particles are partitioned into natural elements defined by grain structure and (e) coupling of the continuum mechanics solution inside a grain with interfacial solution.

an inter-particle potential by preserving the same elastic constants for both systems. More details of the method can be found in [31].

We reemphasize that the ''particle'' in ''Quasi-particle dynamics approach'' is an atomic aggregate and the number of atoms in the aggregate is determined by the scale of interest. It can represent an inclusion particle in alloy matrix such as a TiC particle, or just contains a single atom so that the particle system degenerates to the original crystal.

The ''Quasi-particle dynamics approach'' is developed based on the two distinct methodologies: The embedded-atom method (EAM) [32,33] and meshfree methods [34–36]. Regarding the literatures of meshfree methods and other computational methods associated with multi-scale numerical approaches, we refer to [34,35,37–45]. Review of meshfree methods can be found in [46], also recently in [47,48].

4.1. Pa ˛c ˛ ˛ a ˛ - a ˛c ˛ ˛a

For metals, the EAM [32,33] is a powerful method among those employed in the family of molecular dynamics. In EAM the total energy E_{tot} of a crystal, Figs. 3a or 4a, is expressed as the summation of a combination E_i for each individual atom:

$$E_{tot} = \sum_i E_i, \qquad (4.1)$$

where E_i is defined by

$$E_i = F_i(\rho_i^h) + \frac{1}{2}\sum_{i,j,j\neq i} \Phi_{ij}^{atom}(r_{ij}), \qquad (4.2)$$

where ρ_i^h is the total electron density at atom i associated with the host (i.e., the rest of the atoms in the system) and F_i is a function of ρ_i^h; $\Phi_{ij}^{atom}(r_{ij})$ is a pair-potential that is the function of the distance r_{ij} between atoms i and j.

We propose an addition term to (4.2)

$$E_i = F_i(\rho_i^h) + \frac{1}{2}\sum_{i,j,j\neq i} \Phi_{ij}^{atom}(r_{ij}) + \sum_{\substack{i,j,k,\ j\neq i,k,\\ k\neq i}} G_{ijk}(\theta_{ijk}), \qquad (4.3)$$

where $G_{ijk}(\theta_{ijk})$ is the energy associated with rotation, θ_{ijk} is the angle between bonds i □ j and i □ k.

As suggested in [49], the function F_i $_{i\ \square p}$

Thus, the atomic system in Fig. 10b is completely defined when its crystal structure is given with a fixed

distance of $r_2 = a_0$, eight neighbor atoms at a distance $r_3 = a_0\sqrt{2}$. In order to illustrate the concept, we cut o the ''domain of influence'' of the potentials (4.6) to be less than r_3.

When the crystal is under volumetric deformation

$$a^1 = a^2 = a^3 = a \qquad (4.10)$$

and the bulk modulus at the position that the atom i occupies is

$$K^{atom} = \frac{1}{9a_0}\left(\frac{\partial^2 \Phi^{atomi}}{\partial a_0^2}\right)$$

At the Fe–TiC interface shown in Fig. 3a where Fe is bcc and TiC has the (NaCl)fcc crystal structure, we assume two classes of quasi-particle potentials: the potentials for the bulk Fe or TiC matrix and interfacial potential. Eqs. (4.10)–(4.17) describe the procedure to obtain the quasi-particle dynamics potential of bulk bcc-iron crystal. The TiC matrix is presumed pure elasticity.

The proposed ''equivalent sti ness rule'' is also applied for determining the quasi-particle interfacial potential. The interatomic potential at TiC–Fe interface has already been obtained in Section 3, shown in Figs. 4b and 9. The elastic constant associated with the direction perpendicular to the interface, denoted as $C_{?}^{Fe–TiC}$, is calculated by the second order derivative of (3.1) [13]

$$C_{?}^{Fe\square TiC} \frac{1}{4} \frac{2\gamma_F}{l^{atom}} \frac{d^2 E_N^{\square}}{d\ {}^{2}_{N}} \Bigg|_{TiC–Fe}, \qquad \text{ð4.18Þ}$$

where l^{atom} is the interfacial interplanar spacing of the atomic system at sy/II61Awxc–6–P/PFAFAF–6–ri6

where $_0$ is the density at reference configuration and $\boldsymbol{\tau}$ is the first Piola–Kirchho stress tensor, Ω^{I} is a reference domain that coincides to the grain I in Fig. 10d and e, $\Gamma_{\mathrm{t}}^{\mathrm{I}}$ is the boundary of Ω^{I} where the traction $\bar{\mathbf{t}}$ is applied. In a discretized ''structural particle'' system, the last term in (4.16) is expressed in the form as

$$\int_{\Gamma_{\mathrm{t}}^{\mathrm{I}}} \bar{}$$

- setting up a constitutive model without violation of the energy conservation law
-

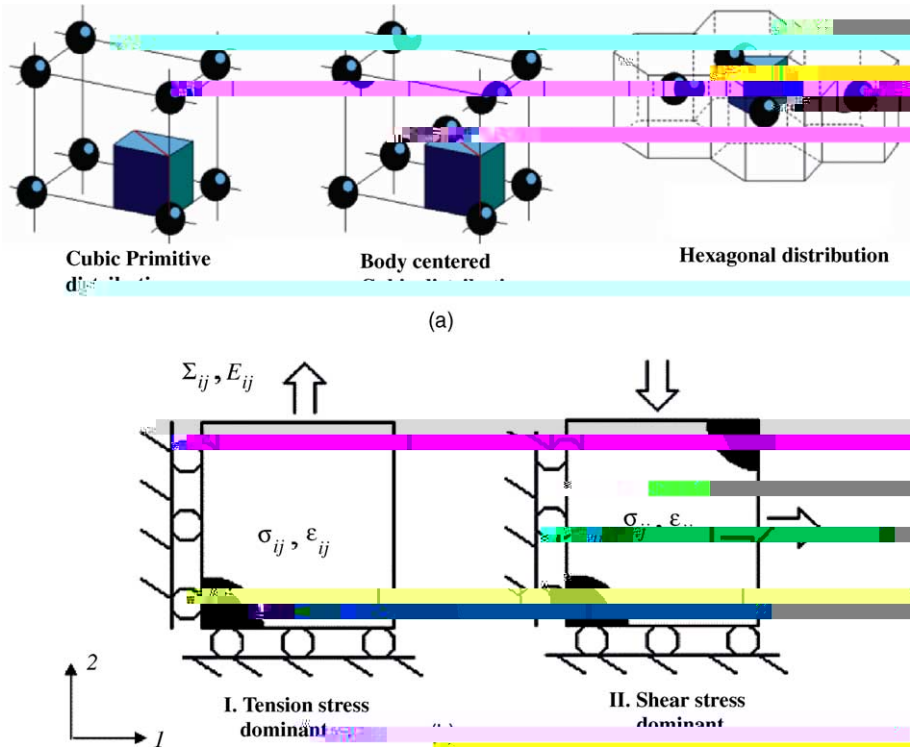

Fig. 11. The cell model: (a) three classes of periodic distributions of inclusions and (b) boundary conditions imposed in cell modeling.

determined by parameters such as the material properties of the cell matrix and inclusion, the interfacial cohesion, the size and geometries of inclusions, and the load imposed on the cell. Both two dimensional and three dimensional cells are analyzed.

5.2.1. S b- c c

The sub-microcell simulation aims to:

(1) investigating the e ects of the secondary inclusion particles (TiC, about 2–300 nm in size) and debonding behavior on the micro-stress–strain response;
(2) establishing the corresponding constitutive model that is applied as the matrix material in a microscale cell model.

The quasi-particle dynamics approach is applied in the sub-microscale cell model. At the structural particles level (Fig. 10d and e), the entire iron matrix is treated as a grain and the inclusions are to be other grains. The interfacial decohesion curves shown in Fig. 9 are applied for establishing the particle potential (4.24). The secondary particle, TiC, is treated as isotropic and linear elastic with the Young's modulus of 600 GPa and a Poisson ratio 0.3.

A crucial part of this simulation is to establish the constitutive law of the iron matrix. According to the first principle calculation, the (1 1 1) adhesion energy of pure iron is about 5.5 J/M^2 which leads to a peak decohesion stress around 45 GPa, see Table 1 and Fig. 12a. When point defects, e.g. empty sites, exist, the adhesion energy drops drastically, see Table 1. Using the homogenization procedure, e.g. [61,87], the

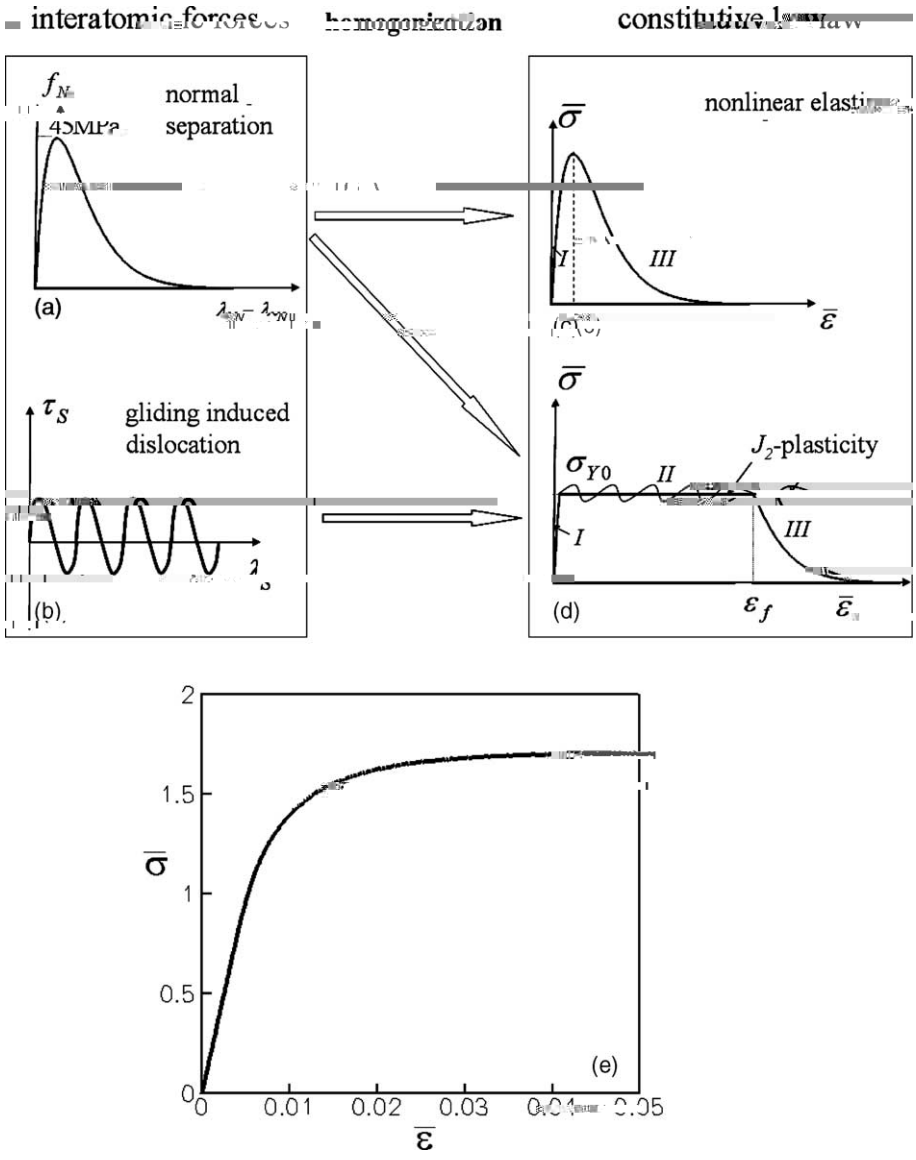

Fig. 12. The constitutive law of iron matrix, from interatomic force-separation relation to conventional plasticity: (a) interatomic normal traction vs. separation; (b) interatomic shear force vs. gliding; (c) a non-linear elasticity, homogenized based on (a); (d) a stress–strain response homogenized combining normal separation and gliding, and J_2 plasticity and (e) experimental measurement of the modified 4340 steel [62,63].

interatomic force separation relation in Fig. 12a can be transformed to an non-linear elastic constitutive law shown in Fig. 12c.

On the other hand, the analysis of Section 3 indicates that a bcc-iron is ''intrinsically ductile'' according to (3.3) and the model introduced in Fig. 5. The corresponding shear traction vs. gliding separation is shown in Fig. 12b. Applying the model illustrated in Fig. 7 to the separation of iron matrix, one can find that the gliding induced dislocation has two obvious e ects on the corresponding homogenized stress–strain

Based on a large amount of numerical simulation and the methodology of cell modeling introduced in

$$\Phi_{\text{plasticity}}(f_0, f, \Sigma_{ij}) = \left(\frac{\bar{\Sigma}}{\Sigma_{\text{intr}}}\right)^2 + A_0 \frac{\Sigma_m}{\Sigma_{\text{intr}}} + A_1(f + g_1)\exp\left(-\frac{\Sigma_m}{\Sigma_{\text{intr}}}\right)$$
$$+ A_2(f + g_2)\exp\left(\frac{\Sigma_m}{\Sigma_{\text{intr}}}\right) - (q_0 + q_1 f^2) = 0, \qquad (5.14)$$

where Σ_{ij}, $\bar{\Sigma}$, Σ_m f_0 and f denote in turn the stress tensor, equivalent stress, mean stress, inclusion and void volume fraction at a given scale; Σ_{intr} denotes the ''material intrinsic strength'' that contains the effects of internal variables associated with strain softening in post-bifurcation stage; the constants A_i and q_i are calibrated through the cell models.

When the constants A_i and q_1

where $\bar{\Sigma}^{\text{micro}}$

possibility of choosing an optimum combination of particle size, geometry and distribution for micro-structural design.

Material resistance against void coalescence is determined by the strength of the ligaments between these voids [88,90]. The deformation tolerance and the failure of the matrix ligament are determined by two basic deformation modes: localization induced necking under normal stress and shear localization caused by the

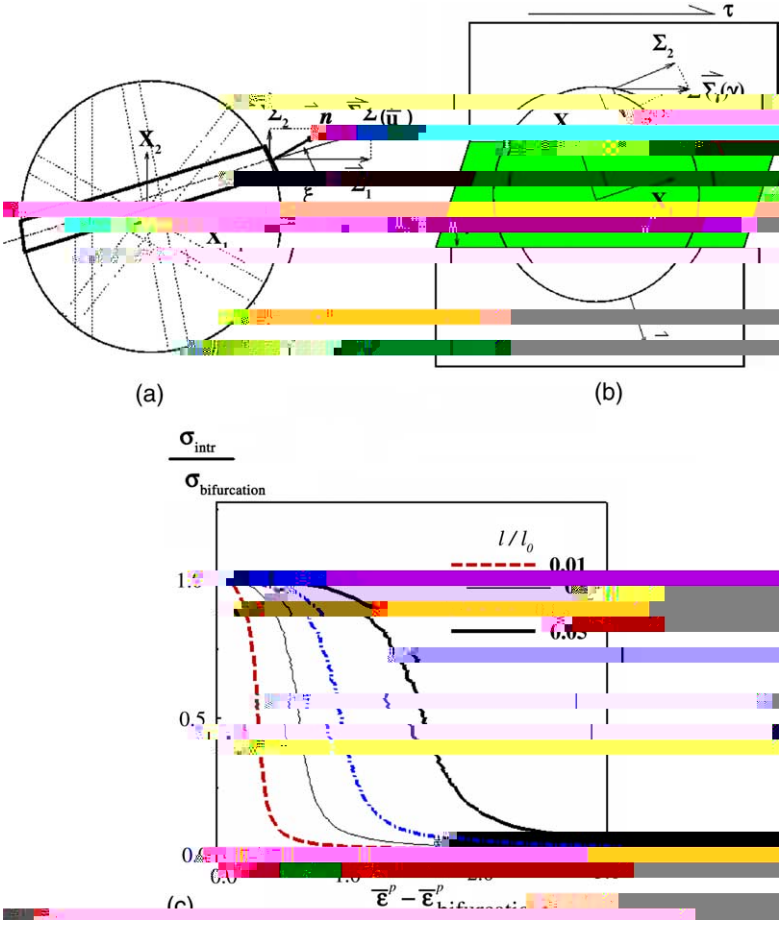

Fig. 19. Two microscopic elements: virtual bond and shear slice.

Table 3
Parameters in (5.19)

A_0	A_1	A_2	g_1	g_2	q_1	q_0
0.0666	0.85	1.7	0.01	0.01	2.65	1.0255

The plastic potential (5.19) is a macroscale, J_2-like plasticity with damage. The concurrent model associated with the mechanisms in Figs. 18 and 19 is described by '' intr'' in (5.19), which is termed ''material intrinsic strength''. It is defined as the combination of a material strain hardening/softening law and the strain gradient-based traction–separation law:

$$\text{intr} = \begin{cases} Y0 \quad \frac{\text{hom}\partial\overline{E}^{p}\text{þ}}{Y0}^{2} \text{ þ } l\eta \text{ strain hardening/softening} & \overline{E}^{p} \leqslant \text{½}\overline{E}\text{□}^{\text{bifurc}}, \\ T\text{ð}Y, l, \eta\text{Þ} \text{ decohesion softening} & \overline{E}^{p} > \text{½}\overline{E}\text{□}^{\text{bifurc}}, \end{cases} \qquad \text{ð5.20Þ}$$

where $\overline{E}^{p}$ is the plastic part of the equivalent strain and $\text{½}\overline{E}\text{□}^{\text{bifurc}}$ denotes $\overline{E}^{p}$ at the bifurcation point of the $_{\text{intr}}\text{ð}\overline{E}^{p}\text{Þ}$ relation. Originally l is defined as the material intrinsic length scale defined as the product of Burger's vector b and the initial yield strength $_{Y0}$; η is the equivalent strain gradient [92]:

$$l = 3\left(\frac{E}{Y_0}\right)^2 b, \quad \eta = \frac{1}{2} u_{k,ij} u_{k,ij}, \tag{5.21}$$

where E is Young's modulus; and the strain-like parameter Y is defined by

$$Y = \left(\bar{E}^p - \left\|\bar{E}\right\|^{bifur}\right) \frac{l}{l_0}, \tag{5.22}$$

where l_0 is a material constant, of the same order as the spacing between primary particles. $\left\|\bar{E}\right\|^{bifurc}$ marks the transition between the two stages of deformation: the uniform deformation with damage nucleation and growth and the failure of the ligaments between these defects. $\left\|\bar{E}\right\|^{bifurc}$ can be calibrated to the maximum stress on the $_{intr}(\bar{E}^p)$ curve from the uniaxial tension test. During the second stage, the e ect of the material intrinsic length scale, strain gradient, and strain rate are incorporated in $_{intr}$ as

$$T = {}_{Y0}\left(T\left(\bar{E}^p, l, l_0\right)\right) \left[\frac{{}_{hom}(\bar{E}^p)}{Y_0}\right]^2 + l\eta. \tag{5.23}$$

The second term in (5.23) is the traction–separation law derived from the strain gradient-based localization solution at the microscale; the third and fourth terms reflect, in turn, the strain rate e ect and the material

Fig. 20 presents two snapshots of 3D crack propagation using the macroscale plastic potential described in (5.19). Fig. 21a shows the contours of equivalent plastic strain around a blunted crack tip at small-scale yielding, where the Rice-Johnson type crack tip strain field is present. Fig. 21b shows the contours after considerable crack growth with large deformation. In this computation the primary particles (TiN) are explicitly embedded into the matrix that includes the secondary particles so that the microscale plastic potential (5.14), in conjunction with the (4.24) in quasi-particle dynamics approach, is applied. Plotted in Fig. 21c is the corresponding load–CTOD curve, where a black square indicates the CTOD at crack initiation which defines the fracture toughness of the material. Figs. 20 and 21 demonstrates that the computational approach is capable of capturing this class of phenomenon. On the other hand, it also reveals that the computational results depend upon many factors such as the geometry and distribution of inclusions, which are not readily captured by the periodic cell models in Fig. 11.

6.2. D c ac a a - -a a a a

The hierarchical constitutive and computational methodology introduced in this paper results in a ''ductile fracture simulator'', illustrated in Fig. 22. Starting from the left-lower corner, the quantum mechanics analysis explores the fundamental atomistic–electronic structures of the alloy matrix and the matrix/inclusion interface. This provides the corresponding energy–adhesion relations that are applied in the sub-micro and microcell modeling to obtain the corresponding constitutive relations (5.14), (5.15), (5.19) for the matrix material in each scale. For the modified 4340 steel, the computational results have been calibrated by experiments. The constitutive law (5.19) of a inclusion induced voiding/microvoiding steel is implemented into compute codes for calculating crack parameters such as the crack tip opening displacement (COD, see Fig. 21a) and the J-integral using the method introduced in [97,98]. The COD (or J-integral) at crack growth initiation represents the fracture toughness of the material according to the ASTM standard. The simulated results are summarized by the toughness–strength–adhesion (TSA) dia-

adhesion energy results in higher peak decohesion stress. Fig. 23b is the TSA diagram corresponding to the TSA curves presented in Fig. 23a.

In the TSA diagram (Fig. 23b) the dashed lines represent the computed load–COD curves for the center cracked panel under tension. Simulations with values of matrix yield strengths of 500, 700, 900 and 1030 MPa are performed using the proposed hierarchical multi-physics constitutive models (5.14), (5.15) and (5.19). Along each dashed line the circle, delta, solid circle, and triangle denote in turn the CODi (the COD at crack growth initiation), corresponding to the di erent levels of decohesion energy of the interface between the iron matrix and the inclusion particles, illustrated in Fig. 23a. The solid lines indicate the variation of fracture toughness when the decohesion energy is fixed but the strength of the iron matrix is varied. For example, at the decohesion energy of 0.6 J/m^2

$$r^2 V_C(\quad) = -4\pi e^2 q(\quad), \tag{A.9}$$

where the $q(\quad)$ denotes the positive point charges of nuclei at its position $\quad_\alpha$ and the electronic charge density $(\quad)$ in the rest

$$q(\quad) = \begin{cases} Z_r & \text{at } \quad_\alpha, \\ (\quad) & \text{otherwise.} \end{cases}$$

The exchange-correlation potential $_{XC}(\quad)$ is related to the exchange-correlation energy that can not solved directly in the same way as $V_C(\quad)$. Under the ''local density approximation'' (LDA) the explicit form of $_{XC}(\quad)$ has been derived, e.g. in [103,104]

$$_{XC}(\quad) = -2\left(\frac{3}{\pi}\right)^{1/3} - 0.0225\,\mathrm{Log}\left(1 + 21\left(\frac{4}{3}\right)^{1/3}\right). \tag{A.10}$$

One way to solve (A.7) is to expand the unknown wave function solutions $_i(\quad)$ as a linear combination of a set of known function with unknown coefficients c_{ij}

$$_i(\quad) = \sum_j c_{ij}\phi_i(\quad). \tag{A.11}$$

Substituting (A.11) into (A.7) leads to the following matrix problem:

$$[\overline{\mathbf{H}} - \epsilon S]\{\quad\} = \mathbf{0}, \tag{A.12}$$

where $\overline{\mathbf{H}}$ is the Hamiltonian matrix and S is the overlap matrix

$$[\overline{H}_{ij}] = \int \phi_i^{\square} \cdot H \cdot \phi_j \, dr; \quad [S_{ij}] = \int \phi_i^{\square}\phi_j \, dr \tag{A.12a}$$

in the first relation of (A.12a) the H is defined by (A.7).

The solution procedure is illustrated in Fig. 24.

In a periodic structure such as a crystal, according to Bloch theorem the wave function solution $_i$ depends upon both position vector and the reciprocal vector

$$_i(\quad + m\mathbf{G}) = e^{i\,\square G}\,{}_i(\quad), \tag{A.13}$$

where **G** is the primitive vector of the lattice and m is an integer. The corresponding electron density yields the integration over the first Brillouin zone:

$$(\quad) = \int_{1^{st}BZ} \vartheta[E_F - \varepsilon_i(\quad)]\,|\,{}_i(\quad)|^2 d\quad, \tag{A.14}$$

where the step function ϑ insures that only occupied states below the Fermi energy E_F are counted.

App i B. C - t t f i t i t f i t

The co-rotational formulation introduced in [60,105] is applied in the analysis presented in this work. We use bold-faced to represent the coordinate of a material point in a reference coordinate system, i.e. the Lagrange configuration; and bold-faced to represents the coordinate of a point in the spatial (Euler) coordinate system. Obviously

$$= (\quad, t). \tag{B.1}$$

Consider a line element vector d_0 in the reference configuration, after deformation it becomes the line element d in the spatial configuration. The deformation gradient is defined by

$$\mathbf{F}(\ , t) = —$$

In numerical analysis, when a body deforms from step n to step n þ 1, its spatial coordinate ^{nþ1} may be written as a function of the configuration at step n and the step length Δt

$$^{nþ1} ¼ {}^{nþ1}ð\ {}^{n}, \Delta tÞ \qquad \text{ðB.7Þ}$$

The displacement increment of this point over the step is

$$\Delta\ ¼ {}^{nþ1} \square\ {}^{n}. \qquad \text{ðB.8Þ}$$

An incremental form of the velocity gradient defined in Eq. (B.5) is

$$\text{ł} ¼ \frac{1}{\Delta t}\frac{\partial \Delta}{\partial\ {}^{nþ1}}. \qquad \text{ðB.9Þ}$$

Thus, we have

$$\frac{\partial}{\partial} \left[\frac{\partial}{\partial} \right]^{-1} . \qquad \text{(B.18)}$$

Appendix C. Elastic-plastic deformation (5.1)

In a co-rotation coordinate system introduced in Appendix B, the rotation part is removed and the deformation can be divided into two steps: pure elastic transformation $\mathbf{F}^e$ and plastic transformation $\mathbf{F}^p$ [109]

$$\mathbf{F} = \mathbf{F}^p \cdot \mathbf{F}^e$$

Following the procedure giving in [60], the velocity gradient l of the deformation field (B.1), defined as the mass derivative of $\mathbf{F}$, is

$$l = \frac{D\mathbf{F}}{Dt} = \frac{\partial \mathbf{F}}{\partial t} \cdot \mathbf{F}^{-1} = \dot{\mathbf{F}} \cdot \mathbf{F}^{-1}, \qquad \text{(C.1)}$$

which has two parts

$$\dot{\mathbf{F}} \cdot \mathbf{F}^{-1} = \dot{\mathbf{F}}^e \cdot \mathbf{F}^p \cdot (\delta \mathbf{F}^e \cdot \mathbf{F}^p)^{-1} + \mathbf{F}^e \cdot \dot{\mathbf{F}}^p \cdot (\delta \mathbf{F}^e \cdot \mathbf{F}^p)^{-1} = \dot{\mathbf{F}}^e \cdot (\delta \mathbf{F}^e)^{-1} + \mathbf{F}^e \cdot \dot{\mathbf{F}}^p \cdot (\delta \mathbf{F}^p)^{-1} \cdot (\delta \mathbf{F}^e)^{-1} \qquad \text{(C.2)}$$

In this paper, we assume that elastic deformation is infinitesimal so that

$$\mathbf{F}^e = \mathbf{I} + \frac{\partial}{\partial} = \mathbf{I} + o(\mathbf{I}), \quad (\delta \mathbf{F}^e)^{-1} = \mathbf{I} - o(\mathbf{I})$$

and

$$l = \dot{\mathbf{F}} \cdot \mathbf{F}^{-1} - \dot{\mathbf{F}}^e \cdot (\delta$$

[41] W.K. Liu, Y.F. Zhang, M.R. Ramirez, Multiple scale finite element methods, Int. J. Numer. Methods Engrg. 32 (1991) 960–990.
[42] L. Ghosh, K. Lee, P. Raghavan, A multi-level computational model for multiscale damage analysis in composite and porous materials, Int. J. Solids Struct. 38 (14) (2001) 2335–2385.
[43] S. Hao, H.S. Park, W.K. Liu, Moving particle finite element method, In. J. Numer. Methods Engrg. 53 (8) (2002) 1937–1958.
[44] G.J. Wagner, W.K. Liu, Coupling of atomistic and continuum simulations using a bridging scale decomposition, J. Computat. Phys. (accepted).
[45] L.E. Shilkrot, W.A. Curtin, R.E. Miller, A coupledatomistic/continuum model of defects in solids, J. Mech. Phys. Solids 50 (10) (2002) 2085–2162.
[46] T. Belytschko, Y. Krongauz, D. Organ, M. Fleming, P. Krysl, Meshless methods: An overview and recent developments, Comput. Methods Appl. Mech. Engrg. 139 (1–4) (1996) 3–47.
[47] S.F. Li, W.K. Liu, Meshfree and particle methods and their applications, Appl. Mech. Rev. 55 (2002) 1–34.
[48] T.-P. Fries, H.G. Matthies, Classification and overview of meshfree methods, Tech. University of Braunschweig, Brunswick, Germany, March 2003.
[49] D.J. Oh, R.A. Johnson, Simple embedded atom method model for Fcc and Hcp metals, J. Mater. Res. 3 (3) (1988) 471–478.
[50] J.H. Rose, J.R. Smith, F. Guinea, J. Ferrante, Universal features of the equation of state of metals, Phys. Rev. B 29 (6) (2002) 2963–2969.
[51] R.A. Johnson, D.J. Oh, Analytic embedded atom method model for Bcc metals, J. Mater. Res. 4 (5) (1989) 1195–1201.
[52] M.F. Horstemeyer et al., A multiscale analysis of fixed-end simple shear using molecular dynamics, crystal plasticity, and a macroscopic internal state variable theory, Model. Simulat. Mater. Sci. Engrg. 11 (3) (2003) 265–286.
[53] N.W. Ashcroft, N.D. Mermin, Solid State Physics, Saunders College Publishing, 1976.
[54] E.B. Tadmor, M. Ortiz, R. Phillips, Quasicontinuum analysis of defects in solids, Philos. Mag. A—Phys. Cond. Matter Struct. Defects Mech. Propert. 73 (6) (1996) 1529–1563.
[55] M. Ortiz et al., Mixed atomistic continuum models of material behavior: The art of transcending atomistics and informing continua, MRS Bull. 26 (3) (2001) 216–221.
[56] S. Hao, W.K. Liu, D. Qian, Localization-induced band and cohesive model, J. Appl. Mech.—Trans. ASME 67 (4) (2000) 803–812.
[57] H.S. Park, W.K. Liu, An introduction and tutorial on multiple scale analysis in solids, Computat. Methods Appl. Mech. Engrg. (accepted).
[58] D. Qian, J. Wagner, W.K. Liu, A multi-scale projection method for the analysis of carbon nanotubes, Computat. Methods Appl. Mech. Engrg. (accepted).
[59] W.K. Liu, K., E.G., Zhang, S., Park, H.S., An introduction to computational nanomechanics and materials, Comput. Methods Appl. Mech. Engrg. (2003) (accepted).
[60] T. Belytschko, W.K. Liu, B. Moran, Nonlinear Finite Elements for Continua and Structures, John Wiley, Chichester New York, 2000, xvi, 650.
[61] P. Zhang et al., The elastic modulus of single-wall carbonnanotubes: a continuum analysis incorporating interatomic potentials, Int. J. Solids Struct. 39 (13-14) (2002) 3893–3906.
[62] G.B. Olson, K.C. Hsieh, Technical Report, Department of Mater Science Engineering, Northwestern University, 2002.
[63] C.L. Briant, et al., Void nucleation in a low alloy steel, in: TMS Meeting. 2002.
[64] J.D. Eshelby, Elastic inclusions and inhomogeneities, in: I.N. Sneddon, R. Hill (Eds.), Progress in Solid Mechanics, North-Holland, Amsterdam, 1961, pp. 89–140.
[65] R. Hill, Continuum micro-mechanics of elastoplastic polycrystals, J. Mech. Phys. Solids 13 (1965) 89–101.
[66] J.W. Hutchinson, Elastic–plastic behaviour of polycrystalline metals and composites, Proc. R. Soc. London Ser. A—Math. Phys. Sci. 319 (1537) (1970) 247.
[67] J.R. Rice, D.M. Tracey, On the ductile enlargement of voids in triaxial stress field, J. Mech. Phys. Solids 17 (1969) 2–15.
[68] A.L. Gurson, Continuum theory of ductile rupture by void nucleation and growth: Part I—Yield criteria and flow rules for porous ductile media, J. Engrg. Mater. Technol. 99 (1977) 2–15.
[69] V. Tvargaard, J.W. Hutchinson, On localization in ductile materials containing spherical voids, Int. J. Fract. 18 (1982) 237–252.
[70] S. Socrate, D.M. Parks, 1995, MIT, Cambridge.
[71] A.S. Khan, Y. Parikh, A study of 2 incremental theories of plasticity through large deformation in polycrystalline copper, Engrg. Fract. Mech. 21 (4) (1985) 697–707.
[72] B. Moran, R.J. Asaro, C.F. Shih, E ects of material rate sensitivity and void nucleation on fracture initiation in a circumferentially cracked bar, Met. Trans. 22A (1991) 161–170.
[73] J.D. Embury, Damage and failure processes in structural-materials, J. Phys. IV 3 (C7) (1993) 607–619.
[74] J.M. Duva, Hutchinson, Constitutive potentials for dilutely voided non-linear materials, J. Mech. Mater. 3 (1984) 41–54.
[75] A.G. Evans, M.C. Lu, S. Schmauder, M. Ruhle, Some aspects of the mechanical strength of ceramic metal bonded systems, Acta Metal. Mater. 34 (8) (1986) 1634–1655.